Noninvasive Nanoscopy Uncovers the Impact of the Hierarchical Porous Structure on the Catalytic Activity of Single Dealuminated Mordenite Crystals

Alexey V. Kubarev,[a] Kris P. F. Janssen,[b] and Maarten B. J. Roeffaers*[a]

Spatial restrictions around catalytic sites, provided by molecular-sized micropores, are beneficial to reaction selectivity but also inherently limit diffusion. The molecular transport can be enhanced by introducing meso- and macropores. However, the impact of this extraframework porosity on the local nanoscale reactivity is relatively unexplored. Herein we show that the area of enhanced reactivity in hierarchical zeolite, examined with super-resolution fluorescence microscopy, is spatially restricted to narrow zones around meso- and macropores, as observed with focused ion-beam-assisted scanning electron microscopy. This comparison indicates that reagent molecules efficiently reach catalytic active sites only in the micropores surrounding extraframework porosity and that extensive macroporosity does not warrant optimal reactivity distribution throughout a hierarchical porous zeolite.

Nanoporosity[1] ensures an optimal interaction between a heterogeneous solid catalyst and a reaction mixture.[1] The resulting large specific surface area, in combination with a high density of active sites, enables the effective use of the entire catalyst particle volume. Depending on their diameter, pores can play several important roles in the heterogeneous catalytic process. Molecular-sized micropores provide spatial restrictions for reagent and/or product molecules around the catalytic active site, and this gives rise to the unique ability to control the reaction outcome on the basis of molecular dimensions. Ideally, these pores are an inherent feature of the crystalline framework ordering, as this would lead to reproducible and uniform pore dimensions, as in the case of zeolites. Such shape-selective zeolite catalysts are widely employed in numerous industrial processes.[3,4]

However, an inherent drawback of these molecular sieve catalysts is restricted diffusion, which often leads to suboptimal crystal volume utilization and accelerates catalyst aging.[5] These intracrystalline diffusion limitations can be overcome through the introduction of larger extraframework meso- and macroporosity into the solid catalyst, which enhances the effectiveness.[6] Perturbation of the periodic crystal structure during creation of a hierarchical porous catalyst can, however, also cause undesired changes in the catalyst's properties or affect the catalytic reaction conditions. For example, at the level of the catalyst's properties, decreased structure density and modifications of the chemical composition can lead to a decrease in the density of active sites. At the reaction level, there is a possibility of side reactions occurring on active sites in the larger extraframework pores, which leads to partial loss of micropore-induced shape selectivity. Whereas the overall effect of meso- and macropore introduction on catalytic performance has thoroughly been investigated at the ensemble-averaged scale level,[6] the direct impact of extraframework porosity on the local, nanoscale reactivity remains relatively unexplored.[7] Nonetheless, small-scale, microscopy-based investigations seem especially essential in view of several recent studies, which revealed the major impact of structural and compositional heterogeneities on the catalytic performance within and between individual catalyst particles.[7–15]

Dealuminated mordenite zeolites are well-known and widely used hierarchical porous catalysts.[16,17] In addition to the intrinsic unidimensional framework microporosity of the mordenite zeolite structure,[18,19] postsynthetic dealumination can further introduce extraframework meso- and macroporosity.[20,21] It is commonly assumed that such extraframework porosity provides more efficient access to the inner micropore volume. However, single-crystal studies of these materials are few, and none have made the direct link between extraframework pore structure and local catalytic activity.[22–25] For these reasons, dealuminated mordenite can be considered an ideal model

---

[1] Porosity-describing terms are used according to IUPAC recommended classification: "micropores" for pore sizes up to 2 nm, "mesopores" for sizes of 2–50 nm, and "macropores" for pores larger than 50 nm.[2] "Nanopores" is used as an overarching term for all pores with a size in the nanometer range (up to 100 nm). Extraframework porosity refers to meso- and macropores that are not part of the zeolite's crystal structure and that, in this case, are introduced by postsynthetic zeolite modification.

[a] A. V. Kubarev, Prof.Dr. M. B. J. Roeffaers
Centre for Surface Chemistry and Catalysis
Faculty of Bioscience Engineering
KU Leuven
Kasteelpark Arenberg 23, 3001 Heverlee (Belgium)
E-mail: maarten.roeffaers@biw.kuleuven.be

[b] Dr. K. P. F. Janssen
Department of Chemistry
Faculty of Sciences
KU Leuven
Celestijnenlaan 200 F, 3001 Heverlee (Belgium)

Part of a Special Issue on Advanced Microscopy and Spectroscopy for Catalysis. A link to the Table of Contents will appear here once the Special Issue is assembled.

system for the nanoscale study of hierarchical porous systems. To reveal the effect of the extraframework porosity on the local catalytic activity, we opted to apply two complementary microscopy techniques. Direct extraframework porosity visualization inside a zeolite crystal was performed by scanning electron microscopy (SEM) assisted by focus ion-beam (FIB) milling; this approach is particularly suited for detailed structural characterization of catalyst particles not transparent to the electron beam.[7, 26, 27] Next, the local catalytic activity was imaged by confocal and super-resolution fluorescence microscopy at the single crystal and single catalytic turnover levels.

For this study, we employed an industrially produced dealuminated synthetic acid mordenite sample. High-resolution SEM is in its nature a surface characterization technique that does not allow the direct exploration of the dealumination-induced extraframework porosity inside a zeolite crystal. For this reason, we resorted to focused ion-beam milling to slice the zeolite crystal in a very precise way, thus exposing the interior of the material for SEM observation (Figure 1). A diagonal section of the crystal was made with a beam of Ga^+ ions (Figure 1 B). Magnification of the freshly uncovered crystal interior reveals an extensive system of macropores running throughout the crystal (Figure 1 C, D).
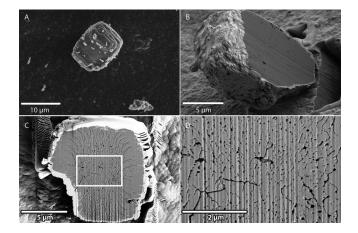

Figure 1. SEM images of A) the intact dealuminated mordenite crystal and B) the side view, C) the front view (white rectangle indicates area of panel D), and D) a highly magnified front view of the FIB-cut dealuminated mordenite crystal. Note that some curtaining effect of the FIB sectioning is visible as straight lines running from the top to the bottom of the crystal section.

In contrast to multiple earlier single-crystal studies, for which a random and irregular orientation of meso- or macropores in hierarchical zeolites was seen,[22–25, 28–30] in this crystal the similarly highly and randomly porous core is complemented by distinct radial pores extending from the center of the crystal to its edges. Next, 10 consecutive images were acquired by shaving approximately 3 nm per slice of the exposed zeolite surface by using the FIB, which allowed evolution of the local 3 D extraframework porosity to be traced and represented (Figure S1, Supporting Information). The observed bimodal pore-size distribution is likely a result of uneven dealumination conditions for different parts of the crystal.

One could expect extended extraframework macroporosity to result in an improved catalytic performance of the zeolite crystals' interior as a result of strongly enhanced molecular transport. However, depletion of framework aluminum might offset this beneficial effect, as a loss in the associated acid sites could result in a reduction in catalytic performance. Moreover, the observed bimodal pore distribution might give rise to a more complicated situation, such as limited accessibility of the potentially active core by diffusion of the reagent through radial pores.

To investigate the effects of dealumination and the resulting extraframework porosity on catalytic performance at a scale compatible with the previous SEM nanoscopy, we relied on super-resolution fluorescence microscopy. The local activity inside catalyst particles can be resolved by monitoring the fluorescence signal originating from the conversion of fluorogenic reactants into fluorescent reaction products.[8, 14, 31–40] Furfuryl alcohol was used as reactant because it fits inside the mordenite framework micropores and because acid-catalyzed oligomerization leads to the formation of fluorescent oligomers.[32, 41] We focused on the initial reactivity, as we were interested in the impact of the enhanced molecular transport in the extraframework porosity on the catalytic performance; all fluorescent microscopy observations were performed within the first 20 min after reagent addition. Further, this minimized the effect of pore blocking by formed reaction products. Confocal laser-scanning microscopy (CLSM) allows the fluorescence intensity in a 1 μm thick layer of a crystal to be measured and, hence, allows the local catalytic performance to be evaluated (Figure 2).

The measured activity profile closely matches the porosity pattern observed with FIB-SEM. Stepwise shifting of the focal plane allows the intracrystal activity distribution throughout the whole crystal volume to be observed. The uncovered 3 D reactivity profile also shows similar activity patterns throughout the entire crystal (Figure 2 A). According to previous research, we know that acid site distribution in such crystals does not follow the observed fan-shaped linear pattern.[10] Therefore, these results clearly show that the entire crystal volume is not available for reactant molecules despite the extensive extraframework porosity. Although the observed elongated zones of catalytic activity follow the same pattern as the extraframework pores, the resolution of the CLSM is diffraction limited and prohibits accurate zone size estimation. Furthermore, the registered fluorescent intensity is not linearly dependent on the chemical reaction rate owing to uneven accumulation of fluorescent product and variance in the number of emitted photons per molecule.

To address these issues, we applied nanometer accuracy by stochastic chemical reactions (NASCA) microscopy, which is super-resolution fluorescence microscopy that enables direct reactivity quantification. NASCA microscopy relies on the mathematical localization of single fluorescent reaction products to circumvent the diffraction-limited resolution of typical far-field fluorescence microscopy.[41–43] This localization enables accurate pinpointing of the reaction product molecule down to a precision of 10 nm. By registering the exact locations of successive,
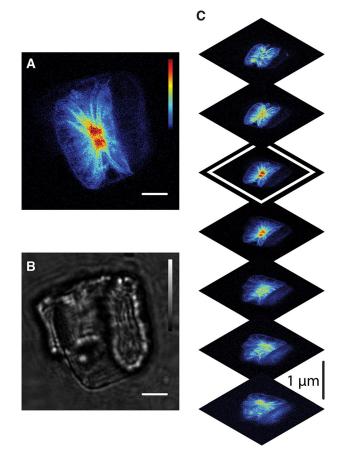
Figure 2. Confocal laser-scanning microscopy microphotograph of furfuryl alcohol oligomers obtained and accumulated within the mordenite crystal. A) Fluorescence image slice (middle of the crystal, depth of field is approximately 800 nm). B) Transmission image. C) Optical sectioning of the crystal. Z-scan was performed with a step size of 1 μm in the axial direction. The white border outlines the slice presented in large in panel B. False color scale shows the observed fluorescence intensity, scale bar: 3 μm.

veals that these highly active zones have a characteristic width of (110 ± 40) nm (Figure 3 B).

This size is larger than the localization precision, which ranges from 10 to 50 nm, and this indicates that active zones might correspond to either the macropores or to the microporous zones of the crystal that border the mesopores. Therefore, the question as to where the reaction happens—in the extraframework macropores or in the original micropores of the mordenite structure—remains unanswered. In an effort to distinguish between both possibilities, we used polarization-resolved fluorescence microscopy measurements, which yield direct insight into the spatial orientation of the product molecules with respect to the underlying pore system. To this end, we used linear polarized excitation light instead of typical circular polarization (Figure 4). Compared to the situation for which the excitation light polarization was perpendicular to the micropores direction (Figure 4 E, F), linearly polarized light parallel to the crystal's micropores could excite 4.1 times more molecules (Figure 4 C, D). Thus, most of the fluorescent reaction product molecules are observed in the micropores, in which they are highly aligned. In contrast, reactivity inside the extraframework pores, in which molecular orientation is more randomized, is limited (Figure 4 B, D, F). This observation agrees well with the previously reported results of polarization-resolved fluorescence microscopy investigation of other dealuminated mordenite crystals.[10] However, it was never shown that the observed activity takes place along the micropores directly outlining the distinct extraframework pores. Additionally, it can be seen that circularly polarized light of the same intensity excites molecules less efficiently than linearly polarized light parallel to the micropores because of the reduced probability of absorption (Figure 4 A, B).

Our results show that the reagent molecules can only reach catalytic active sites in close vicinity of the extraframework po-

individual reaction events, it becomes possible to distinguish between active and inactive zones at the nanoscale on the basis of differences in their observed catalytic activity.

The reactivity map, obtained from this NASCA approach, is presented in Figure 3 A for a representative crystal sample, along with the bright-light transmission image of the same crystal in Figure 3 C. These reactivity maps are 2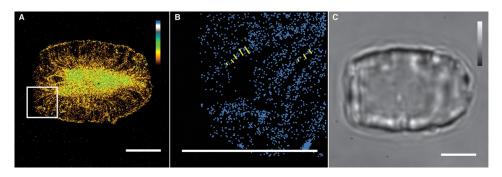D histograms of the distributions of the localized emitters, reconstructed in 50×50 nm^2 bins. Additional examples can be found in Figure S2. Similar to the CLSM measurements, the spatial reactivity pattern matches the extraframework porosity pattern observed by FIB-SEM. Precise analysis of the scatter plot of localized catalytic turnovers inside the zeolite crystal re-

Figure 3. Optical microscopy investigation of furfuryl alcohol conversion inside a mordenite crystal. Scale bars: 3 μm. A) NASCA reactivity map obtained for $50 \times 50 \times 800$ nm^3 voxels (*xyz*) for the duration of 500 s; false color scale shows the observed relative reaction rate; white rectangle indicates area enlarged in panel B. B) Magnification showing the scatter plot with locations of individual reaction events; yellow lines indicate distances taken for region width estimation. C) Corresponding bright-field optical transmission image.

rosity. The results prove that the common belief that the existence of macropores will invariably result in full accessibility to the inner microporous structure is not always correct. Even a hierarchical porous structure with seemingly extensive macroporosity can lead to suboptimal reactivity distribution through-
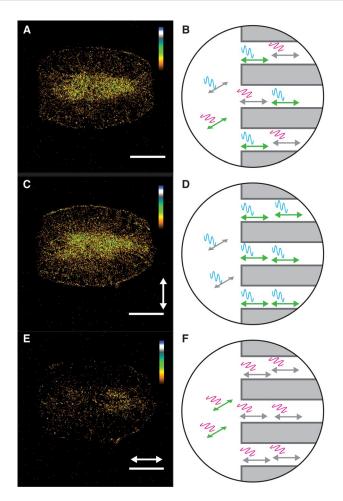
Figure 4. Excitation polarization resolved wide-field fluorescence microscopy investigation of furfuryl alcohol conversion inside a mordenite crystal. Scale bars: 3 μm. NASCA reactivity maps obtained for $50 \times 50 \times 800$ nm^3 voxels (*xyz*) for the duration of 150 s; false color scale indicates observed relative reaction rate. A) NASCA reactivity map obtained with circular polarization of excitation light. C,E) NASCA reactivity maps obtained with linear polarization of excitation light; white arrows indicate the light polarization. B,D,F) Schematic representation of light-fluorophore interaction in the experiments presented in A, C, and E, respectively. Cyan and magenta waves indicate photons with different orientation of polarization plane, green/gray arrows stand for excited/not excited fluorophore molecules.

out a crystal. This degree of insight into the catalytic activity can only be obtained by correlating detailed structural information, for example, from electron microscopy, with high-resolution molecular insight generated by super-resolution fluorescence microscopy. Such single-crystal-level studies provide a solid basis for the rational design of catalysts.

Acknowledgements

[1] M. E. Davis, *Nature* **2002**, *417*, 813–821.
[2] *Pure Appl. Chem.* **1976**, *46*, 71–90.
[3] N. Mizuno, M. Misono, *Chem. Rev.* **1998**, *98*, 199–218.
[4] J. Čejka, G. Centi, J. Perez-Pariente, W. J. Roth, *Catal. Today* **2012**, *179*, 2–15.
[5] P. Magnoux, P. Cartraud, S. Mignard, M. Guisnet, *J. Catal.* **1987**, *106*, 242–250.
[6] J. Pérez-Ramírez, C. H. Christensen, K. Egeblad, C. H. Christensen, J. C. Groen, *Chem. Soc. Rev.* **2008**, *37*, 2530–2542.
[7] L. R. Aramburo, et al., *Chem. Eur. J.* **2011**, *17*, 13773–13781, see Supporting Information.
[8] M. H. F. Kox, E. Stavitski, J. C. Groen, J. Pérez-Ramírez, F. Kapteijn, B. M. Weckhuysen, *Chem. Eur. J.* **2008**, *14*, 1718–1725.
[9] R. Ameloot, F. Vermoortele, J. Hofkens, F. C. De Schryver, D. E. De Vos, M. B. J. Roeffaers, *Angew. Chem. Int. Ed.* **2013**, *52*, 401–405; *Angew. Chem.* **2013**, *125*, 419–423.
[10] K. Liu, A. V. Kubarev, J. Van Loon, H. Uji-I, D. E. De Vos, J. Hofkens, M. B. J. Roeffaers, *ACS Nano* **2014**, *8*, 12650–12659.
[11] L. R. Aramburo, S. Teketel, S. Svelle, S. R. Bare, B. Arstad, H. W. Zandbergen, U. Olsbye, F. M. F. de Groot, B. M. Weckhuysen, *J. Catal.* **2013**, *307*, 185–193.
[12] L. Sommer, S. Svelle, K. P. Lillerud, M. Stöcker, B. M. Weckhuysen, U. Olsbye, *Langmuir* **2010**, *26*, 16510–16516.
[13] I. L. C. Buurmans, B. M. Weckhuysen, *Nat. Chem.* **2012**, *4*, 873–886.
[14] M. B. J. Roeffaers, R. Ameloot, A. J. Bons, W. Mortier, G. De Cremer, R. De Kloe, J. Hofkens, D. E. De Vos, B. F. Sels, *J. Am. Chem. Soc.* **2008**, *130*, 13516–13517.
[15] K. P. F. Janssen, G. De Cremer, R. K. Neely, A. V. Kubarev, J. Van Loon, J. A. Martens, D. E. De Vos, M. B. J. Roeffaers, J. Hofkens, *Chem. Soc. Rev.* **2014**, *43*, 990–1006.
[16] X. Tu, M. Matsumoto, T. Matsuzaki, T. Hanaoka, Y. Kubota, J.-H. Kim, Y. Sugi, *Catal. Lett.* **1993**, *21*, 71–75.
[17] J. Lecomte, A. Finiels, P. Geneste, C. Moreau, *J. Mol. Catal. A* **1998**, *133*, 283–288.
[18] W. M. Meier, *Z. Kristallogr.* **1961**, *115*, 439–450.
[19] P. Simoncic, T. Armbruster, *Am. Mineral.* **2004**, *89*, 421–431.
[20] N. S. Nesterenko, F. Thibault-Starzyk, V. Montouillout, V. V. Yuschenko, C. Fernandez, J.-P. Gilson, F. Fajula, I. I. Ivanova, *Microporous Mesoporous Mater.* **2004**, *71*, 157–166.
[21] K. Lee, B. Ha, *Microporous Mesoporous Mater.* **1998**, *23*, 211–219.
[22] H. Ajot, J. F. Joly, J. Lynch, F. Raatz, P. Caullet, *Stud. Surf. Sci. Catal.* **1991**, *62*, 583–590.
[23] A. J. Koster, U. Ziese, A. J. Verkleij, A. H. Janssen, K. P. de Jong, *J. Phys. Chem. B* **2000**, *104*, 9368–9370.
[24] J. C. Groen, T. Sano, J. A. Moulijn, J. Pérez-Ramírez, *J. Catal.* **2007**, *251*, 21–27.
[25] Y. Jin, Y. Li, S. Zhao, Z. Lv, Q. Wang, X. Liu, L. Wang, *Microporous Mesoporous Mater.* **2012**, *147*, 259–266.
[26] L. Karwacki, D. A. M. De Winter, L. R. Aramburo, M. N. Lebbink, J. A. Post, M. R. Drury, B. M. Weckhuysen, *Angew. Chem. Int. Ed.* **2011**, *50*, 1294–1298; *Angew. Chem.* **2011**, *123*, 1330–1334.
[27] S. Mitchell, N.-L. Michels, K. Kunze, J. Pérez-Ramírez, *Nat. Chem.* **2012**, *4*, 825–831.
[28] A. H. Janssen, A. J. Koster, K. P. de Jong, *J. Phys. Chem. B* **2002**, *106*, 11905–11909.

[29] J. Lynch, F. Raatz, P. Dufresne, *Zeolites* **1987**, *7*, 333 – 340.

[30] C. Choi-Feng, J. B. Hall, B. J. Huggins, R. A. Beyerlein, *J. Catal.* **1993**, *140*, 395 – 405.

[31] G. De Cremer, B. F. Sels, D. E. De Vos, J. Hofkens, M. B. J. Roeffaers, *Chem. Soc. Rev.* **2010**, *39*, 4703 – 4717.

[32] M. B. J. Roeffaers, B. F. Sels, H. Uji-i, B. Blanpain, P. L'hoëst, P. A. Jacobs, F. C. De Schryver, J. Hofkens, D. E. De Vos, *Angew. Chem. Int. Ed.* **2007**, *46*, 1706 – 1709; *Angew. Chem.* **2007**, *119*, 1736 – 1739.

[33] M. R. Decan, S. Impellizzeri, M. L. Marin, J. C. Scaiano, *Nat. Commun.* **2014**, *5*, 4612.

[34] T. Cordes, S. A. Blum, *Nat. Chem.* **2013**, *5*, 993 – 999.

[35] E. M. Hensle, S. A. Blum, *J. Am. Chem. Soc.* **2013**, *135*, 12324 – 12328.

[36] W. Xu, J. S. Kong, Y.-T. E. Yeh, P. Chen, *Nat. Mater.* **2008**, *7*, 992 – 996.

[37] N. M. Andoy, X. Zhou, E. Choudhary, H. Shen, G. Liu, P. Chen, *J. Am. Chem. Soc.* **2013**, *135*, 1845 – 1852.

[38] N. M. Esfandiari, et al., *J. Am. Chem. Soc.* **2010**, *132*, 15167 – 15169, see Supporting Information.

[39] N. M. Esfandiari, S. A. Blum, *J. Am. Chem. Soc.* **2011**, *133*, 18145 – 18147.

[40] P. Chen, X. Zhou, N. M. Andoy, K.-S. Han, E. Choudhary, N. Zou, G. Chen, H. Shen, *Chem. Soc. Rev.* **2014**, *43*, 1107 – 1117.

[41] M. B. J. Roeffaers, et al., *Angew. Chem. Int. Ed.* **2009**, *48*, 9285 – 9289; *Angew. Chem.* **2009**, *121*, 9449 – 9453, see Supporting Information.

[42] M. B. J. Roeffaers, B. F. Sels, H. Uji-I, F. C. De Schryver, P. A. Jacobs, D. E. De Vos, J. Hofkens, *Nature* **2006**, *439*, 572 – 575.

[43] P. Dedecker, S. Duwé, R. K. Neely, J. Zhang, *J. Biomed. Opt.* **2012**, *17*, 126008.